Simulated equinoctial asymmetry of the ionospheric vertical plasma drifts

Zhipeng Ren,[1] Weixing Wan,[1] Jiangang Xiong,[1] and Libo Liu[1]

Received 22 June 2011; revised 23 October 2011; accepted 2 November 2011; published 4 January 2012.

[1] This paper studies the influence of the lower thermospheric tidal winds below 105 km on the equinoctial asymmetry of the equatorial vertical $\mathbf{E} \times \mathbf{B}$ plasma drifts ($V_\perp$) using Theoretical Ionospheric Dynamo Model II of the Institute of Geology and Geophysics, Chinese Academy of Sciences (TIDM-IGGCAS-II) and tidal winds below 105 km from thermosphere-ionosphere-mesosphere-energetics-dynamics satellite Doppler Interferometer (TIDI) observations. Although a series of other nonmigrating tides also affect the $V_\perp$ asymmetry, the simulated equinoctial asymmetry in $V_\perp$ are mainly driven by the migrating diurnal tide (DW1), migrating semidiurnal tide (SW2), DE3, and DW2 nonmigrating tides. The asymmetry in daytime $V_\perp$ varies with local time and longitude and mainly shows three features. First, the simulated daytime $V_\perp$ during the March equinox is larger than that during the September equinox in most of longitudinal sectors. This asymmetry is mainly driven by the semiannual oscillation (SAO) of the migrating diurnal tide in the tropical mesosphere-lower thermosphere (MLT) region, and the equinoctial asymmetry of the migrating semidiurnal tide also plays an important role in the generation of this asymmetry. Second, the daytime $V_\perp$ asymmetry in the Eastern Hemisphere is more significant than that in the Western Hemisphere. Our simulation suggests that the longitudinal variations of the geomagnetic fields and DW2 tides play important roles in the generation of this hemisphere difference. Third, there is an obvious wave number 4 longitudinal structure in the $V_\perp$ asymmetry. Our simulation suggests that this wave number 4 structure is mainly driven by the equinoctial asymmetry of the DE3 tide.

Citation: Ren, Z., W. Wan, J. Xiong, and L. Liu (2012), Simulated equinoctial asymmetry of the ionospheric vertical plasma drifts, *J. Geophys. Res.*, *117*, A01301, doi:10.1029/2011JA016952.

1. Introduction

[2] The ionospheric equinoctial asymmetry, with some ionospheric parameters being larger during one equinox than that during the other one, is an important feature of ionospheric seasonal variation. Since *Titheridge* [1973] first studied such asymmetry in the mid-latitude ionospheric electron density, many researchers had found the ionospheric equinoctial asymmetry in a series of ionospheric density parameters, such as total electron content (TEC), topside ionospheric electron density, ionospheric electron density profiles, and low-latitude ionospheric wave number 4 structures [e.g., *Bailey et al.*, 2000; *Unnikrishnan et al.*, 2002; *Zhao et al.*, 2007; *Wan et al.*, 2008; *Liu et al.*, 2010]. Based on the observations of the incoherent scatter radars (ISRs) and of the satellites, similar asymmetry also had been found in other ionospheric parameters, such as the *F* layer height, electron temperatures, ion temperatures, field-parallel drifts and field-perpendicular plasma drifts [e.g., *Titheridge and Buonsanto*, 1983; *Aruliah et al.*, 1996; *Balan et al.*, 1998; *Kawamura et al.*, 2002; *Zhang et al.*, 2004; *Ren et al.*, 2011]. Previous research was mainly related to the ionospheric equinoctial asymmetry in the high latitudes and middle latitudes. Recently, from the ionospheric electron density profiles and TEC data, *Liu et al.* [2010] investigated the behaviors of the daytime ionosphere around equinoxes and found that the equinoctial asymmetry in the ionospheric plasma density during low solar activity is mainly a low-latitude phenomenon.

[3] The equatorial *F* region vertical plasma drifts ($V_\perp$) play an important role in the low-latitude ionospheric dynamics and can control the low-latitude and equatorial ionosphere. Thus, the results of *Liu et al.* [2010] imply that there may be an equinoctial asymmetry in equatorial $V_\perp$. With $V_\perp$ data observed by ROCSAT-1, *Ren et al.* [2011] studied the equinoctial asymmetry of equatorial $V_\perp$ and suggested that such asymmetry can partly explain the equinoctial asymmetry in the daytime low-latitude ionospheric plasma density observed by *Liu et al.* [2010]. The equatorial ionospheric electric fields (or $\mathbf{E} \times \mathbf{B}$ plasma drifts) are mainly driven by *E* and *F* region neutral wind dynamos [e.g., *Heelis*, 2004]. The *E* region dynamo is driven mainly by the tidal winds that come from below, and the *F* region dynamo is driven mainly by neutral winds driven by the in situ heating. Thus, the equinoctial asymmetry in $V_\perp$ should mainly arise from

[1]Beijing National Observatory of Space Environment, Institute of Geology and Geophysics, Chinese Academy of Sciences, Beijing, China.

0148-0227/12/2011JA016952

the asymmetry in the mesosphere-lower thermosphere (MLT) tides and in thermospheric winds.

[4] Previous research suggested that the thermospheric equinoctial asymmetry, as well as such asymmetry in MLT regions, should play important roles in the generation of the ionospheric equinoctial asymmetry [e.g., *Balan et al.*, 1998]. The equinoctial asymmetry in MLT tides and in thermospheric winds had already been found in a series of works [e.g., *Aruliah et al.*, 1996; *Balan et al.*, 1998, 2006; *Liu et al.*, 2003]. For example, *Aruliah et al.* [1996] found a large equinoctial asymmetry in high-latitude thermospheric winds and plasma drifts. With the observations of the peak height of the *F* layer (hmF2) over Wuhan, *Liu et al.* [2003] found that the thermospheric wind magnitude is smaller during the spring equinox than during the autumn equinox. Using the middle and upper atmosphere (MU) radar observations, *Balan et al.* [2006] studied the equinoctial asymmetry in diurnal mean winds, tides, and waves in the MLT region and suggested that thermosphere and MLT regions could be dynamically coupled through mean winds, tides, and waves. Recently, research based on the observations made by the Sounding of the Atmosphere using Broadband Emission Radiometry (SABER) and the thermosphere-ionosphere-mesosphere-energetics-dynamics satellite (TIMED) Doppler Interferometer (TIDI) instruments on board the TIMED satellite has provided new insight into tidal phenomena in MLT regions and has revealed the climatology and the spatiotemporal distributions of the most important tidal components in temperature and zonal and meridional winds, respectively [e.g., *Forbes et al.*, 2006, 2008; *Oberheide et al.*, 2006; *Oberheide and Forbes*, 2008; *Zhang et al.*, 2006]. These scientists studied the climatology of the migrating (sun-synchronous) and nonmigrating (non-sun-synchronous) tides [e.g., *Forbes et al.*, 2006, 2008; *Oberheide et al.*, 2006; *Oberheide and Forbes*, 2008; *Zhang et al.*, 2006; *Pancheva et al.*, 2009] and found some equinoctial asymmetries in these tides. For example, *Mukhtarov et al.* [2009] and *Xu et al.* [2009] studied the semiannual oscillation (SAO) and showed that the migrating diurnal tidal amplitude in the tropical MLT region is largest around two equinoxes (SAO), and the first cycle of the SAO (spring equinox) is stronger than the second cycle (autumn equinox). *Ren et al.* [2011] studied the equinoctial asymmetry of equatorial $V_\perp$ with the data observed by ROCSAT-1 and suggested that the asymmetry in MLT tides may play important roles in the asymmetry of equatorial $V_\perp$. In the present work, we study the equinoctial asymmetry in equatorial $V_\perp$ using the TIDM-IGGCAS-II model and tidal winds from TIMED-TIDI observations. We mainly simulate the influence of the lower thermospheric tidal winds below 105 km on asymmetry in $V_\perp$ and examine the influences of different tide components.

2. Model and Inputs

[5] To simulate the equinoctial asymmetry in equatorial $V_\perp$, we use the Theoretical Ionospheric Dynamo Model (version II) developed at the Institute of Geology and Geophysics, Chinese Academy of Sciences (TIDM-IGGCAS-II) [*Ren et al.*, 2008a]. Through adopting the magnetic apex coordinates, TIDM-IGGCAS-II can simulate ionospheric electric fields in realistic geomagnetic fields. Similar to the simulations by *Ren et al.* [2010], we take an equivalent extrapolation condition at the high latitudinal boundary in the following simulations. An International Geomagnetic Reference Field (IGRF) geomagnetic field is also used in these simulations. The ionospheric dynamo is controlled by the ionospheric electrical conductivity and thermospheric neutral winds. The model electrical conductivity in TIDM-IGGCAS-II is calculated based on the parameters from IRI2000 and MSIS00 empirical models, which are all carried out with $Ap = 4$ and $F_{10.7} = 130$. Similar to those in the work by *Ren et al.* [2010], the input neutral wind fields were obtained from TIDI observations.

[6] TIDI is a limb scanner on board the TIMED satellite and can measure the zonal (eastward) and meridional (northward) components of the neutral winds in MLT regions by monitoring the Doppler shift of the various upper atmosphere airglow layers [*Killeen et al.*, 2006]. It was developed and built at the University of Michigan and has continuously taken data since March 2002. TIDI observations from March 2002 (high solar activity year) to early November 2007 (low solar activity year) are downloaded from the National Center for Atmospheric Research (NCAR) (see http://timed.hao.ucar.edu/tidi). Although tides are known to have a dependence on solar activity partly because of the way that molecular dissipation affects vertical propagation, previous work suggested that the lower-altitude tides do not show obviously solar activity variations [e.g., *Forbes et al.*, 2008]. Thus, we used the averaged tidal wind between 2002 and 2007 in this simulation. The average can also partly remove the variations in the data that are due to variations with periods longer than 60 days.

[7] The TIMED-TIDI data from 20 February to the end of 2007 are used to obtain tidal components of zonal and meridional velocities. The TIMED orbit processes cover 24 h of local time for every 60 days with combined ascending and descending node data. We process the data using consecutive 60 day windows moved forward in time once per day. The data in 60 day windows were averaged in 5 km altitude, 10° latitude, 20° longitude, and 1 h local time bins to obtain $U(t, \lambda, \varphi, z, d)$, $V(t, \lambda, \varphi, z, d)$ in the window centered at d day, where U and V are zonal and meridional velocities, respectively, in the window, $t = 0, 1, 2, \ldots, 23$ h is universal time, and λ, φ, and z are geographical longitude, latitude, and altitude, respectively. Then, by a two-dimensional Fourier transform, the data in each latitude-altitude bin were decomposed into tidal models:

$$\begin{cases} U(\varphi, h, d, t, \lambda) = \sum_{fk} U_{fk}(\varphi, h, d) e^{i2\pi(ft - k\lambda)} \\ V(\varphi, h, d, t, \lambda) = \sum_{fk} V_{fk}(\varphi, h, d) e^{i2\pi(ft - k\lambda)} \end{cases}, \quad (1)$$

where f (= 1, 2, …) is the tidal frequency in cycles/day and k (= 0, ±1, ±2, …) is the longitudinal wave number in the UT frame, which is related to the local time (LT) wave number k', i.e., $k' = |f + k|$. The amplitudes and phases of diurnal and semidiurnal tides can be obtained from complex Fourier spectra $U_{fk}(\varphi, h, d)$ and $V_{fk}(\varphi, h, d)$ The amplitudes and phases obtained with the above method are almost the same as those obtained by using a least squares method [*Wu et al.*, 2008]. Then we use an inverse Fourier transformation to reconstruct zonal tidal winds and meridional tidal winds.

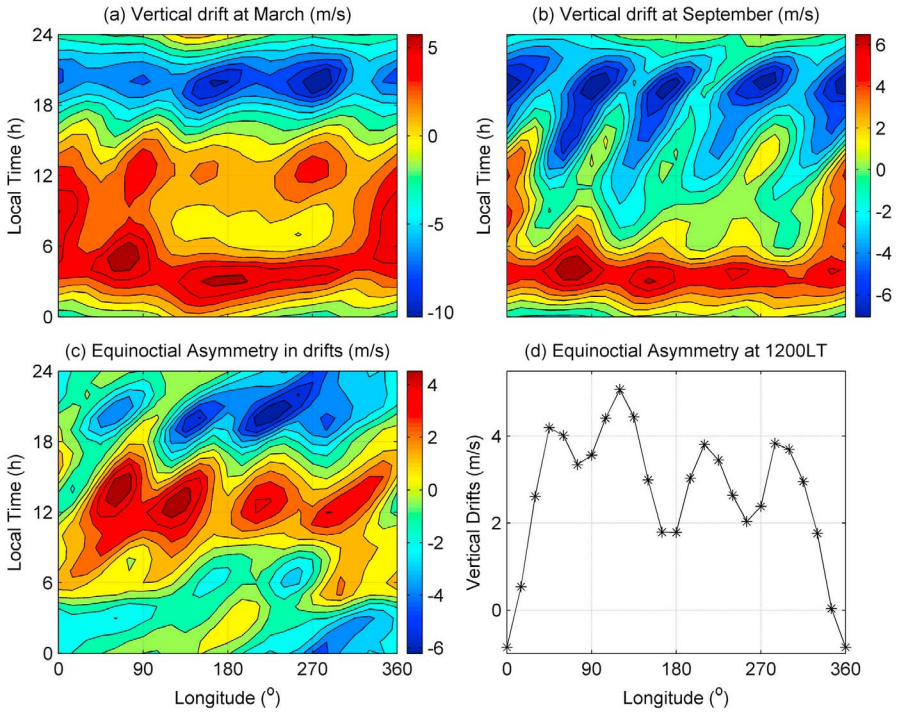

Figure 1. The local time and longitudinal variations of the simulated $V_\perp$ at the height of 600 km for (a) the March equinox and (b) the September equinox; (c) equinoctial asymmetry in $V_\perp$ ($V_{\text{March}} - V_{\text{September}}$) at the height of 600 km, and (d) the longitudinal variations of asymmetry in $V_\perp$ at 1200 LT.

Finally, we obtain the average zonal and meridional winds from 85 to 105 km with a vertical resolution of 5 km and from pole to pole with a latitudinal resolution of 5° for different tidal models during the March equinox and the September equinox. The details of calculations of these tides from TIDI observations can also be seen in the work by *Ren et al.* [2010]. Here, we use the eastward and westward propagating diurnal tides (DEs and DWs) and eastward and westward propagating semidiurnal tides (SEs and SWs) tides in these simulations. The s (s = 1, 2, 3, and 4, s = |*k*|) in Des and DWs and SEs and SWs all describe the zonal wave number in the UT frame.

[8] However, TIDI can provide only the wind below 105 km. Thus, we must set the winds above 105 km. *Ren et al.* [2010] used to simulate the ionospheric wave number 4 structures in equatorial $V_\perp$ based on DE3 tidal winds observed by TIDI. Because of the lack of enough observations, they set the DE3 tidal winds above 105 km to decrease linearly with altitude and become zero above 150 km. However, different tides show different altitudinal variations [*Forbes et al.*, 2008], and a simple description is difficult for describing the complex altitudinal variations of different tides. Thus, we could not use a similar method to provide the higher thermospheric winds. *Ren et al.* [2011] suggested that the semiannual oscillation (SAO) may play an important role in the formation of the equinoctial asymmetry in equatorial $V_\perp$, and the tidal winds in the lower altitude may greatly affect the equinoctial asymmetry. Thus, we use only the tidal winds observed by TIDI in this simulation and set the wind above 105 km to be zero. However, we should notice that the *F* region dynamo and the *E* region dynamo above 105 km play important roles in the generation of the daytime and nighttime ionospheric electric fields (or $\mathbf{E} \times \mathbf{B}$ plasma drifts). Because of the absence of the winds above 105 km, our simulation could not respond well to the diurnal variations of the ionospheric $\mathbf{E} \times \mathbf{B}$ plasma drifts. Hence, we will mainly pay attention to the equinoctial asymmetry in simulated equatorial $V_\perp$ and the influences of different tide components on it.

3. Equinoctial Asymmetry in Equatorial $V_\perp$

[9] We first simulate the equinoctial asymmetry in equatorial vertical $\mathbf{E} \times \mathbf{B}$ plasma drifts ($V_\perp$) driven by all tides together. These tides include the eastward and westward propagating diurnal (DEs and DWs) and semidiurnal (SEs and SWs) tides (s = 1, 2, 3, and 4). With a series of simulations, we get the local time and longitudinal dependences of $V_\perp$ over the dip equator at two equinoxes driven by all tides together. *Ren et al.* [2011] studied the equinoctial asymmetry of equatorial $V_\perp$ at the height of 600 km. Here, we also mainly show simulated $V_\perp$ at the height of 600 km. Figure 1 shows the local time and longitudinal variations of the simulated $V_\perp$ at the height of 600 km for the March equinox (Figure 1a) and for the September equinox (Figure 1b). Because of the lack of the winds and the dynamo processes above 105 km, the simulated $V_\perp$ could not respond well to the diurnal variations of the observed $V_\perp$. Thus, in following sections, we mainly study the simulated $V_\perp$ asymmetry between the March equinox and the September equinox caused by the tidal winds below 105 km. Figure 1c shows the local time and longitudinal variations of $V_\perp$ asymmetry ($V_{\text{March}} - V_{\text{September}}$). To show the details, the longitudinal variations of $V_\perp$ asymmetry at 1200 LT are also shown in

Figure 1d. As there was a lack of F region neutral wind and F region dynamo in the simulations, we could not well simulate the nighttime $V_\perp$, which are mainly driven by the F region dynamo. Thus, we will mainly pay attention to the daytime $V_\perp$ asymmetry.

[10] We notice three features in the daytime $V_\perp$ asymmetry. Notice first that the daytime $V_\perp$ at the March equinox are larger than those at the September equinox in most of longitudinal sectors. The longitudinal average $V_\perp$ asymmetry at 1200 LT is about 3 m/s. As the simulated $V_\perp$ are driven by the E region tidal winds below 105 km, this phenomenon must relate to the equinoctial asymmetry in E region tides, such as the SAO in the tropical MLT region. Previous research suggested that the migrating diurnal tidal amplitude in the tropical MLT region is largest around two equinoxes, and the first cycle of the SAO (spring March equinox) is stronger than the second cycle (autumn September equinox) [e.g., *Dunkerton*, 1982; *Garcia et al.*, 1997; *Mukhtarov et al.*, 2009; *Xu et al.*, 2009]. The stronger migrating diurnal tide can drive a stronger E region dynamo and a stronger equatorial $V_\perp$. We examine the details of this mechanism in the next section.

[11] Second, we notice that the daytime $V_\perp$ asymmetry in the Eastern Hemisphere is more significant than that in Western Hemisphere. As shown in Figure 1d, the average of the $V_\perp$ asymmetry at 1200 LT in the Eastern Hemisphere is about 1.5 m/s larger than that in the Western Hemisphere. *Ren et al.* [2011] also found similar phenomenon in the $V_\perp$ observed by ROCSAT-1. However, they pointed out that asymmetry between the Eastern Hemisphere and the Western Hemisphere can reach nearly 10 m/s, which is obviously larger than our simulated results. This difference may relate to the lack of the winds above 105 km. However, in both the simulation and in the data observed by ROCSAT-1, the asymmetry in the Eastern Hemisphere is more significant than that in the Western Hemisphere. *Ren et al.* [2011] guessed that this difference may be driven by the nonmigrating tide that can drive wave number 1 longitudinal structures, such as DW2, D0, SW3, SW1, sPW1. Actually, equinoctial asymmetries have also be found in the seasonal variations of these tides. For example, *Forbes et al.* [2003] pointed out that the maximum amplitudes of DW2 meridional wind occur during October–November and January–February, and the seasonal variations of DW2 meridional wind show an equinoctial asymmetry. Similar results have also be found by *Forbes et al.* [2008] and *Lu et al.* [2011]. However, we should point out that previous research also suggested that the longitudinal asymmetry in geomagnetic fields can also drive the longitudinal variations in the F region $V_\perp$ [e.g., *Hartman and Heelis*, 2007; *Ren et al.*, 2009b]. Thus, more simulations are needed to study the details of this question, and we examine the influences of different tides on the $V_\perp$ asymmetry in next section.

[12] Third, there is an obvious wave number 4 longitudinal structure in the $V_\perp$ asymmetry, and this wave number 4 structure shifts eastward as local time increases. Recently, the wave number 4 longitudinal structure of EEJ and of equatorial daytime ionospheric vertical plasma drifts at equinox was noticed [e.g., *England et al.*, 2006; *Hartman and Heelis*, 2007; *Kil et al.*, 2007, 2009; *Fejer et al.*, 2008; *Ren et al.*, 2008b, 2009a, 2010; *Pancheva and Mukhtarov*, 2010]. From the $V_\perp$ observed by ROCSAT-1, *Ren et al.* [2011] found a similar structure in the equinoctial asymmetry of equatorial $V_\perp$. They pointed out that the wave number 4 structure near the September equinox appears in the morning and extends into the evening sector, but the structure near the March equinox mainly appears at 0900–1300 LT. Thus, the equinoctial asymmetry in the observed wave number 4 structure mainly appears in the afternoon. As shown in Figure 1c, the simulated wave number 4 structure in $V_\perp$ asymmetry also mainly appears in the afternoon, and the wave number 4 structure in the morning is weaker than that in the afternoon. *Ren et al.* [2010] simulated the wave number 4 structure in $V_\perp$ using the TIDM-IGGCAS-II model and DE3 tidal winds from TIMED-TIDI observations. Their results also showed obvious equinoctial asymmetry. *Ren et al.* [2010] suggested this asymmetry is driven by the asymmetry in the DE3 tide. Actually, a series of research suggested that the DE3 tide shows obviously annual variations and equinoctial asymmetry. For example, *Forbes et al.* [2003] pointed out that the maximum amplitudes of DE3 zonal wind occur during June–October, and the seasonal variations of DE3 zonal wind show an equinoctial asymmetry. Similar results also were found by *Oberheide et al.* [2006], *Forbes et al.* [2008], *Oberheide and Forbes* [2008] and *Ren et al.* [2009a]. Thus, the wave number 4 longitudinal structure in the $V_\perp$ asymmetry may be mainly driven by the asymmetry in DE3 tidal winds.

4. Influence of Different Tides on $V_\perp$ Asymmetry

[13] We also simulated the local time and longitudinal dependences of equatorial $V_\perp$ driven by different tides (including DEs, DWs, SEs, and SWs; s = 1, 2, 3, and 4). As there are too many tides, we study only the most important tides. Figure 2a shows the diurnal and longitudinal averaged amplitudes of the simulated March equinox $V_\perp$ driven by different tides. The x axis shows the wave number, and the asterisks and the circles show the $V_\perp$ amplitude driven by the diurnal and the semidiurnal tides, respectively. As shown in Figure 2a, the $V_\perp$ driven by migrating diurnal (westward propagating diurnal tide with zonal wave number 1, DW1) and semidiurnal (westward propagating semidiurnal tide with zonal wave number 2, SW2) tides are obviously larger than all kinds of nonmigrating tides. In the nonmigrating tides, the DE3 tide drives the largest $V_\perp$. Similar to Figure 2a, Figure 2b shows the simulated averaged $V_\perp$ amplitudes for the September equinox. The $V_\perp$ driven by migrating diurnal (DW1) and semidiurnal (SW2) tides are also larger than all kinds of nonmigrating tides. However, the $V_\perp$ amplitude at the September equinox driven by SW2 is about 0.5 m/s smaller than that at the March equinox. The $V_\perp$ driven by nonmigrating tides also show obvious equinoctial asymmetry. The DE3, DE2, and DW2 tides drive larger $V_\perp$ than the other nonmigrating tides. The $V_\perp$ driven by eastward propagating nonmigrating diurnal tides with zonal wave number 3 (DE3) and driven by westward propagating nonmigrating diurnal tides with zonal wave number 2 (DW2) at the September equinox are larger than those at the March equinox. These asymmetries may mainly relate to the amplitude asymmetry of DE3 and DW2 tides. We should notice that the amplitude difference often could not well describe the $V_\perp$ asymmetry, and the "phase" difference usually also plays an important role. Thus, we show the local time and

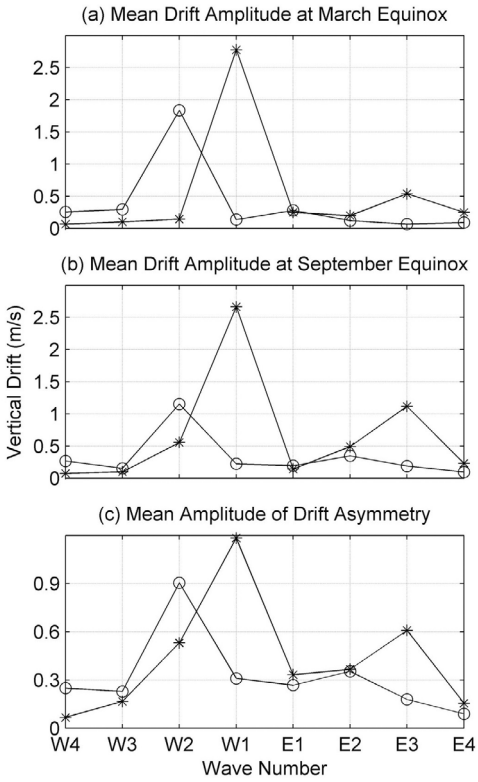

Figure 2. The diurnal and longitudinal averaged amplitudes of the simulated $V_\perp$ driven by different tides at the height of 600 km for (a) the March equinox and (b) the September equinox. (c) The diurnal and longitudinal averaged amplitudes of the $V_\perp$ asymmetry driven by different tides. The x axis is the wave number, and the $V_\perp$ amplitudes driven by the diurnal (asterisks) and semidiurnal (circles) tides are also shown.

longitudinal averaged amplitudes of the $V_\perp$ asymmetry ($V_{\text{March}} - V_{\text{September}}$) driven by different tides in Figure 2c. As shown in Figure 2c, the migrating diurnal tide (DW1) drives the largest $V_\perp$ asymmetry. The asymmetry driven by the migrating semidiurnal tide (SW2) is also larger than that driven by the nonmigrating tides. Although the $V_\perp$ asymmetries driven by DE1, DE2, SE1, and SE2 tides are all strong, the DE3 and DW2 tides drive larger $V_\perp$ asymmetries than the other nonmigrating tides. Thus, we mainly study the influences of DW1, SW2, DE3, and DW2 on the $V_\perp$ asymmetry in the following discussion.

[14] Figures 3a–3d show the $V_\perp$ asymmetry driven by the DW1, SW2, DE3, and DW2 tides, respectively.. Figure 3a shows the local time and longitudinal variations of $V_\perp$ asymmetry driven by the migrating diurnal tide (DW1). We can notice two features in this daytime $V_\perp$ asymmetry. Notice first that the daytime $V_\perp$ at the March equinox are larger than those at the September equinox in most of the longitudinal sectors. This phenomenon should connect with the SAO. Second, there is an obvious asymmetry between the Eastern Hemisphere and the Western Hemisphere, and the equinoctial asymmetry in the Eastern Hemisphere is mainly more significant than that in the Western Hemisphere. This phenomenon may be caused by the longitudinal variations of the geomagnetic fields. Figure 3b shows the local time and longitudinal variations of $V_\perp$ asymmetry driven by the DW2 tide. The daytime $V_\perp$ in the Eastern Hemisphere at the March equinox are mainly larger than those at the September equinox, and the daytime $V_\perp$ in the Western Hemisphere at the March equinox are mainly smaller than those at the September equinox. This asymmetry may mainly relate to the amplitude asymmetry of the DW2 tide. Figure 3c shows the local time and longitudinal variations of the $V_\perp$ asymmetry driven by the migrating semidiurnal tide (SW2). This asymmetry shows obviously semidiurnal variations in all longitudinal sectors. We mainly

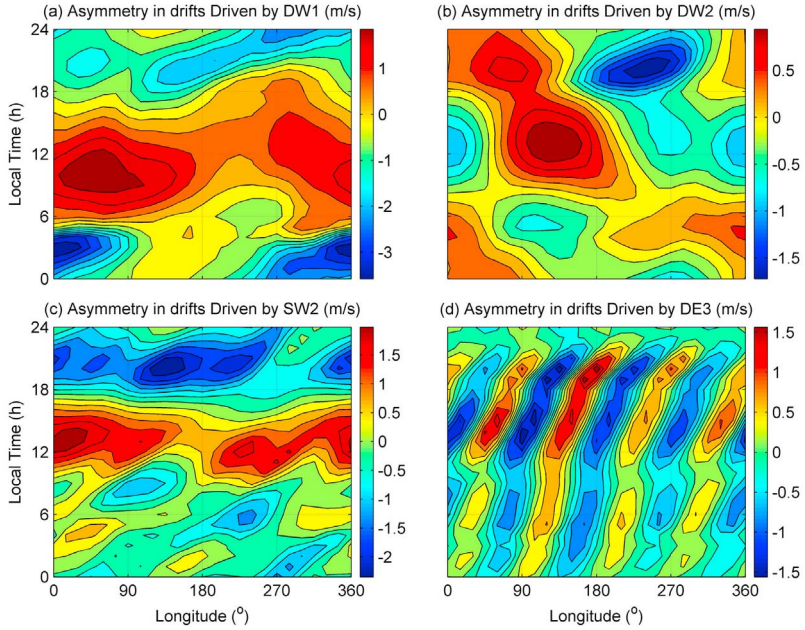

Figure 3. The local time and longitudinal variations of the $V_\perp$ asymmetry ($V_{\text{March}} - V_{\text{September}}$) at the height of 600 km driven by (a) DW1, (b) DW2, (c) SW2, and (d) DE3 tides.

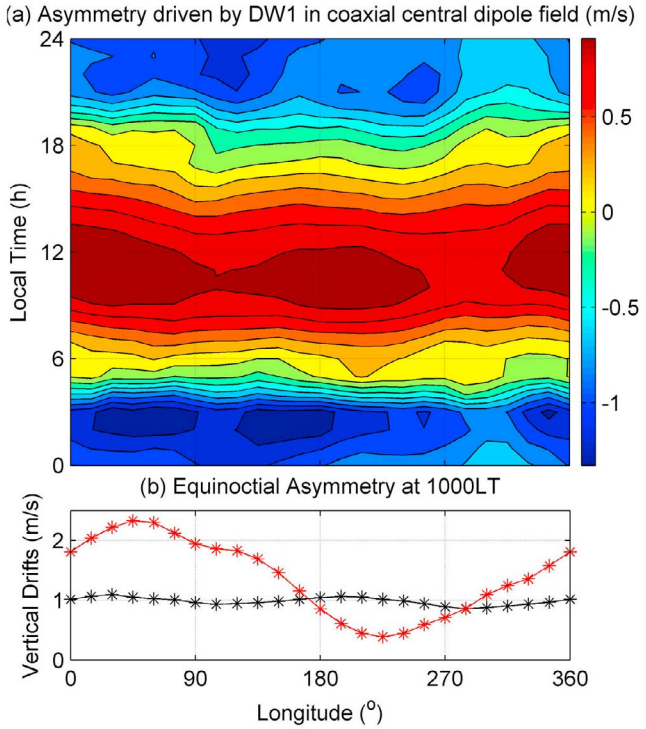

Figure 4. (a) The local time and longitudinal variations of equinoctial asymmetry in $V_\perp$ ($V_{\text{March}} - V_{\text{September}}$) driven by the DW1 tide at the height of 600 km in coaxial central dipole field, and (b) the longitudinal variations of $V_\perp$ asymmetry at 1000 LT in a coaxial central dipole field (black asterisks) and in a realistic geomagnetic field (red asterisks).

pay attention to the daytime asymmetry. As shown in Figure 3c, the morning $V_\perp$ at the March equinox are mainly smaller than those at the September equinox, and the afternoon $V_\perp$ at the March equinox are mainly larger than those at the September equinox. Figure 3d shows the local time and longitudinal variations of $V_\perp$ asymmetry driven by the DE3 tide. This asymmetry shows a wave number 4 longitudinal structure, and this wave number 4 structure shifts eastward as local time increases. We should also notice that the wave number 4 structure in the afternoon is stronger than that in the morning. These results can help us to understand the sources of the simulated daytime $V_\perp$ asymmetry in the third section.

[15] As $V_\perp$ asymmetries driven by the DW1, SW2, DE3, and DW2 tides are obviously larger than those driven by the other tides, the daytime $V_\perp$ asymmetry driven by all tides together should also be mainly controlled by them. Thus, the three features in the total daytime $V_\perp$ asymmetry should also mainly connect with the DW1, SW2, DE3, and DW2 tides. As shown in Figures 3b and 3d, although the DW2 and DE3 both affect the daytime $V_\perp$ asymmetry, the longitudinally averaged daytime asymmetries driven by them are nearly zero. Different from DW2 and DE3, DW1 can drive the more significant daytime $V_\perp$ at the March equinox than those at the September equinox. We should also notice that SW2 can also drive the larger afternoon $V_\perp$ at the March equinox than those at the September equinox. Thus, the DW1 and SW2 both drive the larger daytime $V_\perp$ at the March equinox.

[16] Although the daytime $V_\perp$ asymmetries driven by the DW1, SW2, DE3, and DW2 all show obviously longitudinal variations, it is seen that the SW2 and DE3 tides could not drive the difference between the Eastern Hemisphere and the Western Hemisphere in the daytime $V_\perp$ asymmetry. *Ren et al.* [2011] suggested that this hemisphere difference may be driven by the DW2, D0, SW3, and SW1 tides. Our simulation suggests that the DW1 and DW2 tides play important roles in the generation of this hemisphere difference. The DW2 tide shows a wave number 1 longitudinal structure in the LT frame. Thus, as shown in Figure 3b, it can drive the hemisphere difference. However, DW1 is a migrating tide and does not show longitudinal variations in the LT frame. Hence, the realistic geomagnetic fields may play an important role in this longitudinal asymmetry. To examine this idea, we also simulate the $V_\perp$ driven by the DW1 tide at two equinoxes in a coaxial central dipole field. Figure 4a shows the local time and longitudinal variations of $V_\perp$ asymmetry at the height of 600 km. To show the details, we also compare the longitudinal variations of $V_\perp$ asymmetry at 1000 LT in a coaxial central dipole field (black asterisks) and in a realistic geomagnetic field (red asterisks) in Figure 4b. Because of the longitudinal variations of ionospheric electrical conductivity, $V_\perp$ asymmetry in a coaxial central dipole field also shows some longitudinal asymmetry. However, as shown in Figure 4b, the longitudinal asymmetry in a coaxial central dipole field is obviously weaker than that in a realistic geomagnetic field. Thus, the longitudinal variations of the geomagnetic fields should also play an important role in the generation of hemisphere difference.

[17] *Ren et al.* [2011] found that this is a wave number 4 longitudinal structure in the observed daytime $V_\perp$ asymmetry and suggested that this structure is driven by the equinoctial asymmetry in the DE3 tide. Actually, the equinoctial asymmetry of the wave number 4 structure in the equatorial $V_\perp$ had been found in both observations and simulations [*Ren et al.*, 2009a, 2010]. *Ren et al.* [2011] pointed out that the wave number 4 structure in the September equinox lasts longer than that in the March equinox. We notice that the wave number 4 structure in the afternoon $V_\perp$ asymmetry driven by the DW3 tide (Figure 3d) is stronger than that in the morning. *Ren et al.* [2011] found that the wave number 4 structure in $V_\perp$ exists almost throughout the daytime and even extends into the evening sector at the September equinox, while it appears mainly at noon and prenoon at the March equinox. Thus, the asymmetry of the morning wave number 4 structure must be weaker than that in the afternoon.

5. Summary and Conclusion

[18] In the present work, using the TIDM-IGGCAS-II model and tidal winds below 105 km from TIMED-TIDI observations, we investigate the influence of the lower thermospheric tidal winds below 105 km on the equinoctial asymmetry of the equatorial vertical $\mathbf{E} \times \mathbf{B}$ plasma drifts ($V_\perp$) and examine the influences of different tide components. Although a series of other nonmigrating tides also affect the $V_\perp$ asymmetries, the simulated equinoctial asymmetries are mainly driven by the migrating diurnal tide (DW1), the migrating semidiurnal tide (SW2), and the DE3

and DW2 nonmigrating tides. The asymmetry in the daytime $V_\perp$ varies with local time and longitude and mainly shows three features. First, the simulated daytime $V_\perp$ during the March equinox are larger than those during the September equinox in most of longitudinal sectors. This asymmetry is mainly driven by the semiannual oscillation (SAO) of the migrating diurnal tide in the tropical MLT region, and the equinoctial asymmetry of the migrating semidiurnal tide also plays an important role in the generation of this asymmetry. Second, we notice that the daytime $V_\perp$ asymmetry in the Eastern Hemisphere is more significant than that in the Western Hemisphere, and the longitudinal variations of the geomagnetic fields and DW2 tides play important roles in the generation of this hemisphere difference. . Third, there is an obvious wave number 4 longitudinal structure in the $V_\perp$ asymmetry, and this is mainly driven by the equinoctial asymmetry of the DE3 tide.

[19] **Acknowledgments.** This work is supported by the National Important Basic Research Project (2011CB811405), National Science Foundation of China (41004070, 41131066, 40974090, 40725014), and China Postdoctoral Science Foundation.

[20] Robert Lysak thanks the reviewers for their assistance in evaluating this paper.

References

Aruliah, A. L., A. D. Farmer, T. J. Fuller-Rowell, M. N. Wild, M. Hapgood, and D. Rees (1996), An equinoctial asymmetry in the high-latitude thermosphere and ionosphere, *J. Geophys. Res.*, *101*(A7), 15,713–15,722, doi:10.1029/95JA01102.

Bailey, G. J., Y. Z. Su, and K.-I. Oyama (2000), Yearly variations in the low-latitude topside ionosphere, *Ann. Geophys.*, *18*, 789–798, doi:10.1007/s00585-000-0789-0.

Balan, N., Y. Otsuka, S. Fukao, and G. J. Bailey (1998), Equinoctial asymmetries in the ionosphere and thermosphere observed by the MU radar, *J. Geophys. Res.*, *103*(A5), 9481–9495, doi:10.1029/97JA03137.

Balan, N., S. Kawamura, T. Nakamura, M. Yamamoto, S. Fukao, W. L. Oliver, M. E. Hagan, A. D. Aylward, and H. Alleyne (2006), Simultaneous mesosphere-lower thermosphere and thermospheric *F* region observations using middle and upper atmosphere radar, *J. Geophys. Res.*, *111*, A10S17, doi:10.1029/2005JA011487.

Dunkerton, T. (1982), Theory of the mesopause semiannual oscillation, *J. Atmos. Sci.*, *39*, 2681–2690, doi:10.1175/1520-0469(1982)039<2681:TOTMSO>2.0.CO;2.

England, S. L., S. Maus, T. J. Immel, and S. B. Mende (2006), Longitudinal variation of the *E* region electric fields caused by atmospheric tides, *Geophys. Res. Lett.*, *33*, L21105, doi:10.1029/2006GL027465.

Fejer, B. G., J. W. Jensen, and S.-Y. Su (2008), Quiet time equatorial *F* region vertical plasma drift model derived from ROCSAT-1 observations, *J. Geophys. Res.*, *113*, A05304, doi:10.1029/2007JA012801.

Forbes, J. M., X. Zhang, E. R. Talaat, and W. Ward (2003), Nonmigrating diurnal tides in the thermosphere, *J. Geophys. Res.*, *108*(A1), 1033, doi:10.1029/2002JA009262.

Forbes, J. M., J. Russell, S. Miyahara, X. Zhang, S. Palo, M. Mlynczak, C. J. Mertens, and M. E. Hagan (2006), Troposphere-thermosphere tidal coupling as measured by the SABER instrument on TIMED during July–September 2002, *J. Geophys. Res.*, *111*, A10S06, doi:10.1029/2005JA011492.

Forbes, J. M., X. Zhang, S. Palo, J. Russell, C. J. Mertens, and M. Mlynczak (2008), Tidal variability in the ionospheric dynamo region, *J. Geophys. Res.*, *113*, A02310, doi:10.1029/2007JA012737.

Garcia, R., T. Dunkerton, R. Lieberman, and R. Vincent (1997), Climatology of the semiannual oscillation of the tropical middle atmosphere, *J. Geophys. Res.*, *102*(D22), 26,019–26,032, doi:10.1029/97JD00207.

Hartman, W. A., and R. A. Heelis (2007), Longitudinal variations in the equatorial vertical drift in the topside ionosphere, *J. Geophys. Res.*, *112*, A03305, doi:10.1029/2006JA011773.

Heelis, R. A. (2004), Electrodynamics in the low and middle latitude ionosphere: A tutorial, *J. Atmos. Sol. Terr. Phys.*, *66*(10), 825–838, doi:10.1016/j.jastp.2004.01.034.

Kawamura, S., N. Balan, Y. Otsuka, and S. Fukao (2002), Annual and semiannual variations of the midlatitude ionosphere under low solar activity, *J. Geophys. Res.*, *107*(A8), 1166, doi:10.1029/2001JA000267.

Kil, H., S.-J. Oh, M. C. Kelley, L. J. Paxton, S. L. England, E. Talaat, K.-W. Min, and S.-Y. Su (2007), Longitudinal structure of the vertical **E** × **B** drift and ion density seen from ROCSAT-1, *Geophys. Res. Lett.*, *34*, L14110, doi:10.1029/2007GL030018.

Kil, H., S.-J. Oh, L. J. Paxton, and T.-W. Fang (2009), High-resolution vertical **E** × **B** drift model derived from ROCSAT-1data, *J. Geophys. Res.*, *114*, A10314, doi:10.1029/2009JA014324.

Killeen, T. L., Q. Wu, S. C. Solomon, D. A. Ortland, W. R. Skinner, R. J. Niciejewski, and D. A. Gell (2006), TIMED Doppler interferometer: Overview and recent results, *J. Geophys. Res.*, *111*, A10S01, doi:10.1029/2005JA011484.

Liu, L., X. Luan, W. Wan, J. Lei, and B. Ning (2003), Seasonal behavior of equivalent winds over Wuhan derived from ionospheric data in 2000–2001, *Adv. Space Res.*, *32*(9), 1765–1770, doi:10.1016/S0273-1177(03)90474-1.

Liu, L., M. He, X. Yue, B. Ning, and W. Wan (2010), Ionosphere around equinoxes during low solar activity, *J. Geophys. Res.*, *115*, A09307, doi:10.1029/2010JA015318.

Lu, X., A. Z. Liu, J. Oberheide, Q. Wu, T. Li, Z. Li, G. R. Swenson, and S. J. Franke (2011), Seasonal variability of the diurnal tide in the mesosphere and lower thermosphere over Maui, Hawaii (20.7°N, 156.3°W), *J. Geophys. Res.*, *116*, D17103, doi:10.1029/2011JD015599.

Mukhtarov, P., D. Pancheva, and B. Andonov (2009), Global structure and seasonal and interannual variability of the migrating diurnal tide seen in the SABER/TIMED temperatures between 20 and 120 km, *J. Geophys. Res.*, *114*, A02309, doi:10.1029/2008JA013759.

Oberheide, J., and J. M. Forbes (2008), Tidal propagation of deep tropical cloud signatures into the thermosphere, *Geophys. Res. Lett.*, *35*, L04816, doi:10.1029/2007GL032397.

Oberheide, J., Q. Wu, T. L. Killeen, M. E. Hagan, and R. G. Roble (2006), Diurnal nonmigrating tides from TIMED Doppler Interferometer wind data: Monthly climatologies and seasonal variations, *J. Geophys. Res.*, *111*, A10S03, doi:10.1029/2005JA011491.

Pancheva, D., and P. Mukhtarov (2010), Strong evidence for the tidal control on the longitudinal structure of the ionospheric *F* region, *Geophys. Res. Lett.*, *37*, L14105, doi:10.1029/2010GL044039.

Pancheva, D., P. Mukhtarov, and B. Andonov (2009), Global structure, seasonal and interannual variability of the migrating semidiurnal tide seen in the SABER/TIMED temperatures (2002–2007), *Ann. Geophys.*, *27*(2), 687–703, doi:10.5194/angeo-27-687-2009.

Ren, Z., W. Wan, Y. Wei, L. Liu, and T. Yu (2008a), A theoretical model for mid- and low-latitude ionospheric electric fields in realistic geomagnetic fields, *Chin. Sci. Bull.*, *53*(24), 3883–3890, doi:10.1007/s11434-008-0404-4.

Ren, Z., W. Wan, L. Liu, B. Zhao, Y. Wei, X. Yue, and R. A. Heelis (2008b), Longitudinal variations of electron temperature and total ion density in the sunset equatorial topside ionosphere, *Geophys. Res. Lett.*, *35*, L05108, doi:10.1029/2007GL032998.

Ren, Z., W. Wan, L. Liu, and J. Xiong (2009a), Intra-annual variation of wave number 4 structure of vertical **E** × **B** drifts in the equatorial ionosphere seen from ROCSAT-1, *J. Geophys. Res.*, *114*, A05308, doi:10.1029/2009JA014060.

Ren, Z., W. Wan, L. Liu, R. A. Heelis, B. Zhao, Y. Wei, and X. Yue (2009b), Influences of geomagnetic fields on longitudinal variations of vertical plasma drifts in the presunset equatorial topside ionosphere, *J. Geophys. Res.*, *114*, A03305, doi:10.1029/2008JA013675.

Ren, Z., W. Wan, J. Xiong, and L. Liu (2010), Simulated wave number 4 structure in equatorial *F* region vertical plasma drifts, *J. Geophys. Res.*, *115*, A05301, doi:10.1029/2009JA014746.

Ren, Z., W. Wan, L. Liu, Y. Chen, and H. Le (2011), Equinoctial asymmetry of ionospheric vertical plasma drifts and its effect on *F* region plasma density, *J. Geophys. Res.*, *116*, A02308, doi:10.1029/2010JA016081.

Titheridge, J. E. (1973), The electron content of the southern mid-latitude ionosphere, 1965–1971, *J. Atmos. Terr. Phys.*, *35*, 981–1001, doi:10.1016/0021-9169(73)90077-9.

Titheridge, J. E., and M. J. Buonsanto (1983), Annual variations in the electron content and height of the *F* layer in the northern and southern hemispheres, related to neutral composition, *J. Atmos. Terr. Phys.*, *45*, 683–696, doi:10.1016/S0021-9169(83)80027-0.

Unnikrishnan, K., R. B. Nair, and C. Venugopal (2002), Harmonic analysis and an empirical model for TEC over Palehua, *J. Atmos. Sol. Terr. Phys.*, *64*, 1833–1840, doi:10.1016/S1364-6826(02)00187-6.

Wan, W., L. Liu, X. Pi, M.-L. Zhang, B. Ning, J. Xiong, and F. Ding (2008), Wavenumber-four patterns of the total electron content over the low latitude ionosphere, *Geophys. Res. Lett.*, *35*, L12104, doi:10.1029/2008GL033755.

Wu, Q., D. A. Ortland, T. L. Killeen, R. G. Roble, M. E. Hagan, H.-L. Liu, S. C. Solomon, J. Xu, W. R. Skinner, and R. J. Niciejewski (2008), Global distribution and interannual variations of mesospheric and lower

thermospheric neutral wind diurnal tide: 1. Migrating tide, *J. Geophys. Res.*, *113*, A05308, doi:10.1029/2007JA012542.

Xu, J., A. K. Smith, H.-L. Liu, W. Yuan, Q. Wu, G. Jiang, M. G. Mlynczak, J. M. Russell III, and S. J. Franke (2009), Seasonal and quasi-biennial variations in the migrating diurnal tide observed by Thermosphere, Ionosphere, Mesosphere, Energetics and Dynamics (TIMED), *J. Geophys. Res.*, *114*, D13107, doi:10.1029/2008JD011298.

Zhang, S.-R., J. M. Holt, A. M. Zalucha, and C. Amory–Mazaudier (2004), Midlatitude ionospheric plasma temperature climatology and empirical model based on Saint Santin incoherent scatter radar data from 1966 to 1987, *J. Geophys. Res.*, *109*, A11311, doi:10.1029/2004JA010709.

Zhang, X., J. M. Forbes, M. E. Hagan, J. M. Russell III, S. E. Palo, C. J. Mertens, and M. G. Mlynczak (2006), Monthly tidal temperatures 20–120 km from TIMED/SABER, *J. Geophys. Res.*, *111*, A10S08, doi:10.1029/2005JA011504.

Zhao, B., W. Wan, L. Liu, T. Mao, Z. Ren, M. Wang, and A. B. Christensen (2007), Features of annual and semiannual variations derived from the global ionospheric maps of total electron content, *Ann. Geophys.*, *25*, 2513–2527, doi:10.5194/angeo-25-2513-2007.

L. Liu, Z. Ren, W. Wan, and J. Xiong, Beijing National Observatory of Space Environment, Institute of Geology and Geophysics, Chinese Academy of Sciences, Beijing 100029, China. (zpren@mail.iggcas.ac.cn)